BUILD SIMUL (2010) 3: 3–13
DOI 10.1007/s12273-010-0301-z

Influence of ventilation arrangements on particle removal in industrial cleanrooms with various tool coverage

Yun-Chun Tung[1], Shih-Cheng Hu[1](✉), Tengfang Xu[2], Ren-Huei Wang[1]

1. Department of Energy and Refrigerating Air-Conditioning Engineering, National Taipei University of Technology, 1, Sec. 3, Chung-Hsiao E. Rd., Taipei, 10608, Taiwan, China

2. International Energy Studies Group, Environmental Energy Technologies Division, Lawrence Berkeley National Laboratory, One Cyclotron Road, MS90-3111, Berkeley, CA 94720, USA

Abstract

This paper aims to investigate the influence of comparative ventilation arrangements (wall-return, locally balanced ceiling-return, and four-way ceiling-return) on the airflow distribution and particle fates within cleanrooms of ISO cleanliness class 7 with various tool coverage ratios (0%, 38%, and 60%). Computational fluid dynamics (CFD) was employed to analyze and compare the influence of the three ventilation arrangements on concentrations for particles of various sizes (diameters ranging from 0.01 to 100 μm) in the cleanrooms. The techniques of Eulerian and Lagrangian in CFD were employed for solving the continuous fluid and tracking the particle trajectory, respectively. The outcomes from this study suggested that particle removal rates for the given cleanrooms were significantly affected by the tool coverage ratios, the design of ventilation, and the particle sizes of concerns. In the cases of heavy tool coverage, the locally balanced ceiling-return ventilation arrangements can minimize the need for the relocation of the production lines and layouts of the production tools in cleanrooms, and may provide viable solutions to effective contamination without compromising contamination effectiveness or efficiency.

Keywords

cleanroom,
particle,
CFD,
Lagrangian,
industrial building

Article History

Received: 4 October 2009
Revised: 29 December 2009
Accepted: 3 January 2010

1 Introduction

In a typical industrial cleanroom where particle concentration is controlled, wall-return coupled with recirculation from ceiling is commonly designed and constructed to create non-unidirectional airflows inside the cleanroom. Often, actual production tools installed in cleanrooms may affect the airflow pathway leading to wall-return exits. According to the definition of Airborne Particulate Cleanliness Classes in ISO Standard 14644-1 (1999), air cleanliness class in industrial cleanrooms is associated with the concentration of airborne particles along with diameter of the particles of concern. Equation (1) shows the maximal permitted particle concentration (C_n) in relation with ISO cleanliness class (N), and the associated diameter of the particles of concern (D).

$$C_n = 10^N \times (0.1/D)^{2.08} \quad (1)$$

where C_n is the maximum-permitted number of particles per cubic meter equal to or greater than the specified particle size (D, in μm), with N being the ISO cleanliness class number (a multiple of 0.1 and no more than 9).

In an existing arrangement of airflow path in a cleanroom with ISO cleanliness classes 6 to 8, filtered air is supplied from the ceiling equipped with fan-filter units (FFUs) to create non-unidirectional airflows and returned to the wall grilles that are vertical to the floor. In such a wall-return cleanroom, the directions of airflows could be largely consistent with the movement of settling particles, while the return air shafts (RAS) are normally required. Electric power demand for FFUs can be increased due to long paths of airflows in the recirculation systems (i.e., from the FFU outlets through RAS, then back to the inlets of FFUs) and increased resistance. In addition, the airflow distribution can be significantly influenced by the location and coverage of production tools, devices, and the movements of operators.

E-mail: schu.ntut@gmail.com

List of symbols

F_A	additional force coefficient (m/s^2)	μ	dynamic viscosity (Pa·s)
F_D	drag force coefficient (s^{-1})	ρ	fluid density (kg/m^3)
g	gravitational acceleration (m/s^2)	ϕ	dependent variable
k	turbulence kinetic energy (m^2/s^2)		
P	pressure (Pa)	*Subscripts*	
V	velocity vector (m/s)		
u, v, w	velocity component in the x, y, and z directions, respectively (m/s)	e	effective
		x, y, z	the x, y, and z directions in Cartesian coordinates, respectively (m)
β	thermal expansion coefficient (K^{-1})		
Γ	effective exchange coefficient	p	particle
ε	turbulence kinetic energy dissipation rate (m^2/s^3)	t	turbulent

Murakami et al. (1989) numerically studied the diffusion field of particle contaminants in a cleanroom (ISO cleanliness class 7) with turbulent flows (i.e., non-unidirectional flows). The supply grilles have great influence on the flow fields and also a rather large influence on contaminant diffusion fields. A change in arrangement or in the number of exhaust grilles hardly affects the entire flow field; however, such change often has a large influence on the contaminant diffusion field since the path of contaminant transportation is changed greatly by the position of the exhaust grilles. In addition, Kato et al. (1992) indicated that location changes in return or return arrangement often have large influence on the contaminant diffusion field because of different paths of contaminant transportation. Lu and Howarth (1996) used a numerical model predicting the movements of air and aerosol particle in two interconnected ventilated zones. The particle deposition and migration are mainly influenced by the particle properties, the ventilation conditions and the airflow patterns in the two zones. Particle migrates faster with a high ventilation rate. Larger particles ($d_p = 4$ μm) deposit much faster than smaller particles ($d_p = 2$ μm). Yang et al. (2009) employed computational fluid dynamics (CFD) numerical modeling using Re-Normalization Group (RNG) k-ε method to examine the effects of various ventilation designs for an ISO Class 5 cleanroom on contaminant dispersion and particle concentrations and identified optimal ventilation options confirmed by experimental measurements. Shimada et al. (1996) studied experimentally and theoretically the change in concentration distribution of particulate contaminants emitted in a room to investigate whether the transport of contaminants in a room with a source of particles can be predicted by numerical simulation. The experimental results showed that the concentration distribution depends on the position of introduction of the contaminants. It was also indicated that the contaminants introduced near the room floor diffuse more than those predicted. However, the calculated concentrations agreed almost quantitatively with the measured results, except near the floor and walls. Hu and Tung (2002) used Eulerian and Lagrangian methods to examine the airflow fields and particle fates in non-unidirectional-flow cleanrooms (ISO cleanliness class 7), and have found that a wall-return type cleanroom is less effective in dispatching particles to return/exhaust exits than the locally balanced supply-return airflow rate system (i.e., the exhaust grilles are installed so that the supply and exhaust airflow rates are balanced locally in that space), except that particles generated close to return grilles are more effectively returned from the cleanroom. Zhao and Wu (2005) investigated particle diffusion with gravitational sedimentation in a clean room with different ventilation modes by CFD. The results showed that ventilation mode, particle source location and air exchange rate can influence particle distribution in a clean room.

In industrial buildings, cleanrooms designed with the ceiling-return arrangements normally present less barrier compared with wall-return arrangement, especially considering the needs for relocation of production lines and layouts of the production tools in such facilities. With the increasing application and advancement of FFUs for air recirculation in cleanrooms (Chen et al. 2007; Xu et al. 2007), installing supply and return air grilles on the ceiling become feasible. Such arrangement applied the characteristics of negative pressure within supply-air plenums to facilitate the return air from the interior of the cleanroom to the ceiling grilles.

2 Purpose

In order to identify and develop viable solutions to effective contamination control for critical industrial buildings, this study aimed to examine and compare the performance of three ventilation arrangements: the ceiling-return, the wall-return, and the four-way ceiling-return in non-unidirectional

airflow cleanrooms using Eulerian and Lagrangian methods. The ceiling-return designs have locally-balanced supply and return grilles, i.e., the return grilles are locally located around each supply grille, and the total area of each supply-air-grille opening equals to that of return-air-grille openings around the supply grille. In order to understand compounding effects of tool coverage in the cleanroom, we develop CFD models to simulate the air and particle movement in the cleanroom with three levels of tool coverage and with three ventilation arrangements.

3 Numerical simulation

3.1 Methodology

A control-volume-based technique is used to convert the governing equation into an algebraic equation that can be solved numerically (Fluent 2004). This control volume technique consists of integrating the governing equations about each control volume, yielding discrete equations that conserve each quantity on a control-volume basis. The air movement in the steady flows complies with the principle of conservation and is expressed in general form as follows:

$$\mathrm{div}(\rho V\phi) = \mathrm{div}(\Gamma_\phi \nabla\phi) + S_\phi \tag{2}$$

The diffusion coefficients Γ_ϕ and the source term S_ϕ for each dependent variable ϕ are summarized in Table 1. Field variables (stored at cell centers) must be interpolated to the faces of the control volumes in the finite volume method. The diffusion terms were central-differenced and always second-order accurate. Using the second-order discretization will generally obtain more accurate results. Thus, the second order upwind scheme was used for the treatment of the convection and diffusion-convection terms in the governing equation in the present study. After discretization, the transport equation contains the unknown scalar variable ϕ at the cell center as well as the unknown values in surrounding neighbor cells. This equation, in general, is nonlinear with respect to these variables. A linearized conservation equation for a general variable ϕ at a cell P can be written as follows (Fluent 2004):

$$a_p\phi_p = \sum_{\mathrm{nb}} a_{\mathrm{nb}}\phi_{\mathrm{nb}} + b \tag{3}$$

where the subscript nb refers to neighbor cells, a_p the center coefficient for ϕ, a_{nb} the influence coefficients for the neighboring cells ϕ_{nb}, and b the source term. This results in a set of algebraic equations with a sparse coefficient matrix. For scalar equations, Fluent solves this linear system using a point implicit (Gauss-Seidel) linear equation solver in conjunction with an algebraic multi-grid (AMG) method. The algorithm of semi-implicit method for pressure linked equations (SIMPLE) developed earlier (Patankar 1980), gained the broadest application in the CFD calculation (Kim et al. 2002; Zhai et al. 2004; Chang et al. 2006; Cheong and Phua 2006; Zhang and Chen 2006; Kassomenos et al. 2008), and was used to solve iteratively the pressure-velocity coupling equations in the present study.

Table 1 Variables, diffusion coefficients, and source terms in the governing equations

Equation	ϕ	Γ_ϕ	S_ϕ
Continuity	1	0	0
Momentum	u	$\mu_e = \mu + \mu_t$	$-\frac{\partial P}{\partial x} + \frac{\partial}{\partial x}\left(\mu_e \frac{\partial u}{\partial x}\right) + \frac{\partial}{\partial y}\left(\mu_e \frac{\partial v}{\partial x}\right) + \frac{\partial}{\partial z}\left(\mu_e \frac{\partial w}{\partial x}\right)$
	v	$\mu_e = \mu + \mu_t$	$-\frac{\partial P}{\partial y} + \frac{\partial}{\partial x}\left(\mu_e \frac{\partial u}{\partial y}\right) + \frac{\partial}{\partial y}\left(\mu_e \frac{\partial v}{\partial y}\right) + \frac{\partial}{\partial z}\left(\mu_e \frac{\partial w}{\partial y}\right) - \rho g$
	w	$\mu_e = \mu + \mu_t$	$-\frac{\partial P}{\partial z} + \frac{\partial}{\partial x}\left(\mu_e \frac{\partial u}{\partial z}\right) + \frac{\partial}{\partial y}\left(\mu_e \frac{\partial v}{\partial z}\right) + \frac{\partial}{\partial z}\left(\mu_e \frac{\partial w}{\partial z}\right)$
Kinetic energy	k	$\mu + \frac{\mu_t}{\sigma_k}$	$G_k + G_b - \rho\varepsilon$
Dissipation rate	ε	$\mu + \frac{\mu_t}{\sigma_\varepsilon}$	$C_{1\varepsilon}\frac{\varepsilon}{k}(G_k + C_{3\varepsilon}G_b) - C_{2\varepsilon}\rho\frac{\varepsilon^2}{k}$

where

$G_k = \mu_t S$, $G_b = -g\frac{\mu_t}{\rho Pr_t}\frac{\partial\rho}{\partial y}$, $\mu_t = \rho C_\mu \frac{k^2}{\varepsilon}$, $C_\mu = 0.0845$,

$C_{1\varepsilon} = 1.42$, $C_{2\varepsilon} = 1.68 + \frac{C_\mu \eta^3 (1-\eta/\eta_0)}{1+\beta\eta^3}$, $C_{3\varepsilon} = \tanh\left|\frac{v}{\sqrt{u^2+w^2}}\right|$,

$\sigma_k = \sigma_\varepsilon = 0.7179$, $\beta = 0.012$, $\eta_0 = 4.38$, $\eta = Sk/\varepsilon$,

$S = 2\left[\left(\frac{\partial u}{\partial x}\right)^2 + \left(\frac{\partial v}{\partial y}\right)^2 + \left(\frac{\partial w}{\partial z}\right)^2\right] + \left(\frac{\partial u}{\partial y} + \frac{\partial v}{\partial x}\right)^2 + \left(\frac{\partial u}{\partial z} + \frac{\partial w}{\partial x}\right)^2 + \left(\frac{\partial v}{\partial z} + \frac{\partial w}{\partial y}\right)^2$

A reliable turbulence model, numerical scheme, and numerical algorithm could increase the accuracy of simulation. Turbulence models (Reynolds Averaged Navier-Stokes equations), especially two-equation model, already become the universal used methods in the computation of indoor flow field (Wang et al. 2006). The re-normalization group (RNG) k-ε model has been successfully applied to simulate indoor airflow fields (Feziger and Peric 2002; Yi and Malkawi 2008; Cheng et al. 2009). Chen (1995) compared different k-ε models for indoor air flow computations and reported that the RNG k-ε model is slightly better than the standard k-ε model and is recommended for simulations of indoor air flow. Therefore, the RNG k-ε model was used to

predict the airflow field in the present study.

Moreover, this study judged the convergence not only by examining residual levels, but also by monitoring relevant integrated quantities. All discrete conservation equations are obeyed in all cells to a specified tolerance and solution no longer changes with more iterations. The convergence criterion in this study requires that the scaled residuals decrease to 10^{-3} for all equations in the governing equations except the energy equation, which is not calculated in the present study.

The standard wall functions for the k-ε turbulence model were adopted to link the solution variables at the near-wall cells and the corresponding quantities near the wall. The standard wall functions employed in the present study is based on the proposal of Launder and Spalding that have been extensively used for industrial flows. To resolve reliable turbulence phenomena near the wall, the grid nearest to the wall fell into the logarithmic layer (that is, $y^+ > 30-60$). Moreover, the turbulence kinetic energy k and the turbulence kinetic energy dissipation rate ε employed in air supply and air outlet are calculated by the following equations:

$$k = \frac{3}{2}\left(u_{\text{avg}} I\right)^2 \tag{4}$$

$$\varepsilon = C_{\mu}^{3/4}\left(k^{3/2} l\right) \tag{5}$$

$$l = 0.07 D_{\text{h}} \tag{6}$$

where u_{avg} refers to the mean flow velocity, I the turbulence intensity, D_{h} the hydraulic diameter, and $C_{\mu} = 0.09$.

The trajectory of a discrete phase particle is predicted by integrating the force balance on the particle, which is expressed in a Lagrangian reference frame. This force balance equates the particle inertia with the forces acting on the particle, and can be written (for the x direction in Cartesian coordinates) as follows:

$$\frac{\mathrm{d}u_{\text{p}}}{\mathrm{d}t} = F_{\text{D}}(u - u_{\text{p}}) + g_x(\rho_{\text{p}} - \rho)/\rho_{\text{p}} + F_{\text{A}} \tag{7}$$

Here, the left hand side of the Eq. (7) represents the inertial force per unit particle mass, where u_{p} is the particle velocity vector. $F_{\text{D}}(u - u_{\text{p}})$ refers to the drag force per unit particle mass, where u is the velocity of the air. $g_x(\rho_{\text{p}} - \rho)/\rho_{\text{p}}$ is the force of gravity and the buoyancy on the particle, where ρ and ρ_{p} are the density of the air and the particles, respectively. F_{A} stands for additional forces per unit particle mass that may be important. Note that in order to predict the dispersion of particles due to turbulence, the fluctuating velocity value (u') is added to the instantaneous velocity value (u), i.e., $u = \overline{u} + u'$. The mean velocity ($\overline{u}$), which is the direct output of CFD, determines the convection of the particles along the streamline, while the fluctuating velocity contributes to the turbulent diffusion of particles.

The integration time step (Δt) is computed by FLUENT (Fluent 2004) based on a specified length scale L, and the velocity of the particle (u_{p}) and of the continuous phase (u):

$$\Delta t = L/\left(u_{\text{p}} + u\right) \tag{8}$$

where L is proportional to the integration time step and is defined as the distance that the particle will travel before its motion equations are solved again and its trajectory is updated. The length scale L is set to 0.01 m in the present study. It is for reference that, when we calculated the particle trajectories in a personal computer, CPU: 2.4 GHz-Intel Core 2 Quad Q6600, and Memory: 4 GB-DDR2, the total time required to complete the tracking for particle sizes of 0.01, 0.1, 1, 10, and 100 μm was about 168, 167, 157, 106, and 0.1 min, respectively, in the case of the ceiling-return type cleanroom with the tool coverage ratio of 38%.

3.2 Room models

Figures 1 through 3 show three ventilation arrangements of locally balanced ceiling-return (model A), wall-return (model B), and four-way ceiling-return (model C) employed in the non-unidirectional airflow cleanroom in this study, of which the total area and numbers of supply/return-air grilles are presented in Table 2. The dimensions of each studied cleanroom model are the same: 7.8 m (length) × 3.2 m (height) × 7.8 m (width) in the x, y, and z directions. Second, ventilation systems are all balanced in that the total area of supply-air grilles are the same as that of the return-air grilles in each of the design (i.e., having a total area of 3.24 m^2 openings for supply and return grilles, respectively), while the numbers and locations of return grilles are all different among three designs.

The arrangements of return air grilles in each room model are different in locations and individual grille sizes, while those of supply air grilles are the same, consisting of nine square grilles (each size of 600 mm × 600 mm). In model A (Fig. 1), the supply and the return grilles in the locally balanced ceiling-return cleanroom are arranged in a diamond pattern to catch the rising air streams toward the ceiling exit. In model B (Fig. 2), the wall-return cleanroom has four separate return grilles, located in the opposite walls near the floor and corners, each sizing 600 mm × 1350 mm. In model C (Fig. 3), the four-way ceiling-return cleanroom has four sets of return grilles (each having four long narrow

opening sizing 600 mm × 150 mm). Each set is located around one supply-air grille on the ceiling. For each of the ventilation design, three tool coverage ratios (defined as the floor area occupied by the tools divided by the total cleanroom floor area) are selected: 0%, 38%, and 60%. Figures 1 – 3 show the locations of the tools.

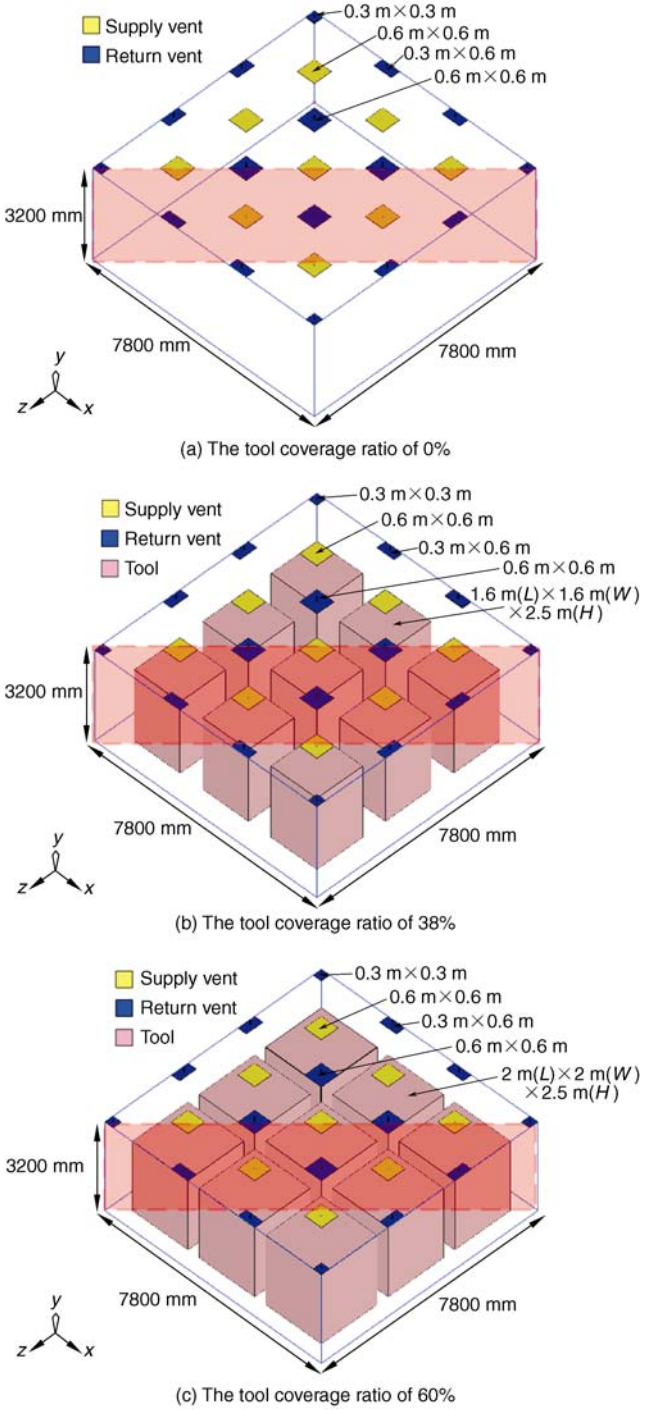

Fig. 1 Model A: a locally balanced ceiling-return ventilation arrangement

Fine meshes could reach a better accuracy than coarse meshes; hence, the present study applied 1 444 268, 1 839 024, and 1 839 024 cells for the models A, B, and C, respectively. The grids and cells are unstructured and hexahedral, and the grid systems reach an independent solution. In model A with the tool coverage ratio of 38%, examples of four grid densities, 435 709 (Case 1), 843 804 (Case 2), 1 155 412 (Case 3), and 1 444 268 (Case 4) cells were exhibited for the

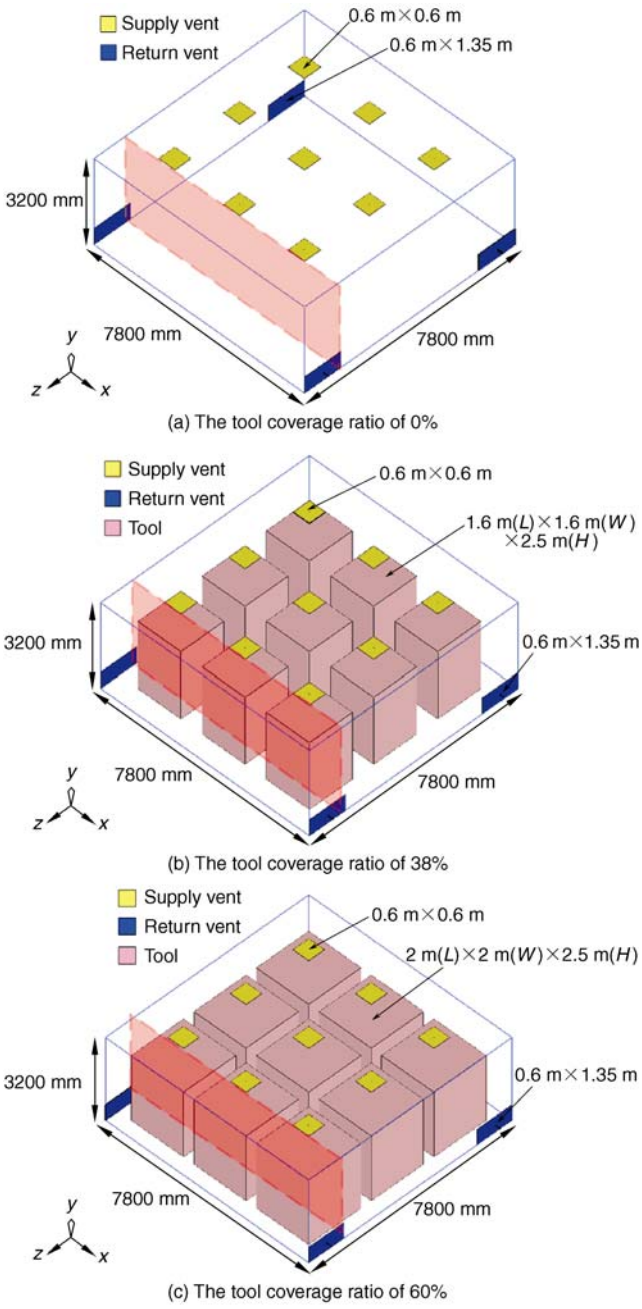

Fig. 2 Model B: a wall-return ventilation arrangement

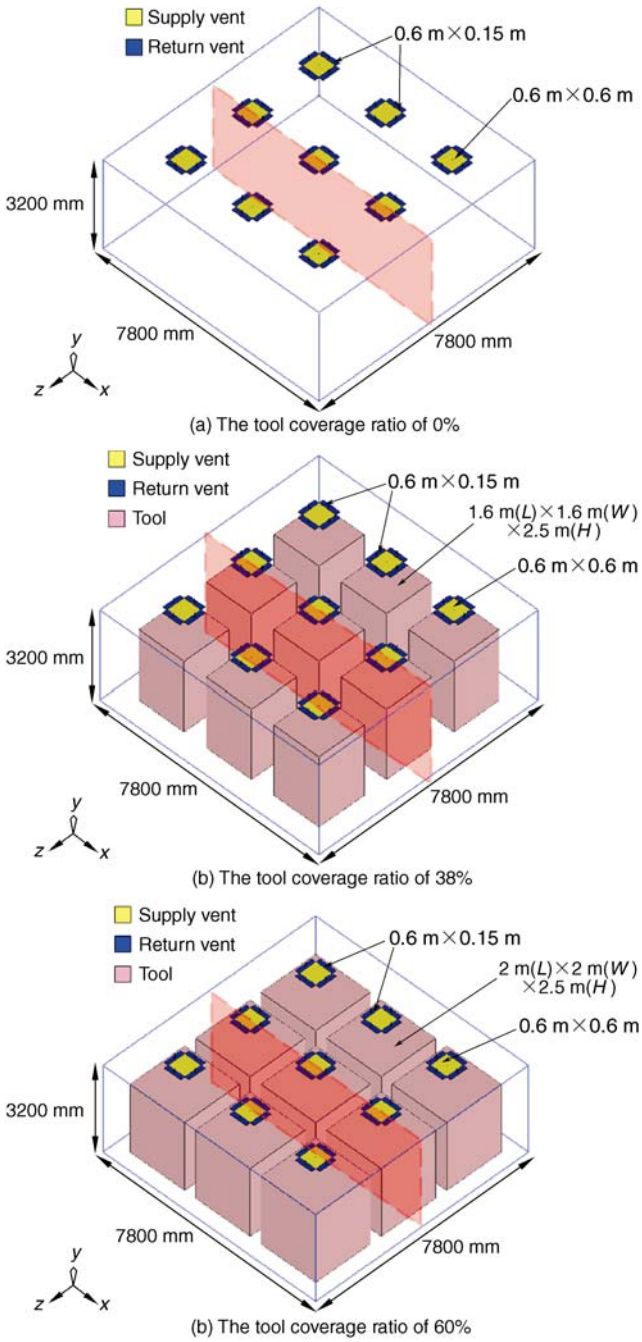

Fig. 3 Model C: a four-way ceiling-return ventilation arrangement

Table 2 Total area and numbers of supply/return-air grilles

Model	Supply grille			Return grille		
	Location	Number	Total area (m^2)	Location	Number	Total area (m^2)
A	Ceiling	9	3.24	Ceiling	16	3.24
B	Ceiling	9	3.24	Wall	4	3.24
C	Ceiling	9	3.24	Ceiling	36	3.24

grid independent study. Figure 4 presents the results of grid independent test; here the velocity magnitude of room air was monitored among points (3.9, 0, 2.7) and (3.9, 3.2, 2.7) in Cartesian coordinates, close to a location of particles generated. The velocity at the monitored points in the case of 1 155 412 cells was quite close to the one in the case of 1 444 268 cells; moreover, the relative error of the average velocity of room air between Cases 1 and 2, Cases 2 and 3, and Cases 3 and 4 reported 3.6%, 3.5%, and 1.0%, respectively. As the difference between Cases 3 and 4 was insignificant, it could be concluded that the grid system reached an independent solution. Therefore, the grid density with 1 444 268 cells was found to be sufficient and applied into the continue study.

3.3 Boundary conditions

Several assumptions are made to simplify the simulation, including (1) incompressible, iso-thermal, and 3D steady-state turbulent flow, (2) spherical solid particles, and (3) no interaction between the continuous and discrete phases. The inlet flow is defined as entering the room with a uniform velocity, $v = -0.35$ m/s. This corresponds to the supply airflow rate of $0.35 \times 3.24 \times 3600 = 4082$ m^3/h, resulting in 21 air changes per hour (ACH $= 4082/(7.8 \times 7.8 \times 3.2)$), higher than the minimal air change rate (i.e., air change rate no less than 20 ACH) for ISO-Cleanliness-Class-7 cleanrooms recommended by IEST-RP-CC012.2 for non-unidirectional airflow (IEST 2007). Neumann boundary conditions are applied at the outlet to satisfy the mass conservation law. A non-slip condition at the solid wall is applied, such that the velocity at its surface is set to zero.

For discrete phase calculations, the diameters of particles are divided into five groups—0.01 μm, 0.1 μm, 1.0 μm, 10 μm, and 100 μm. Predicting the particle fates is at the same base conditions in all studied cases; this study, hence, assumes that the particle source is located fictitiously at $3.9 - 5.0$ m (length), 1.5 m (height), and 2.7 m (width) in the x, y, and z

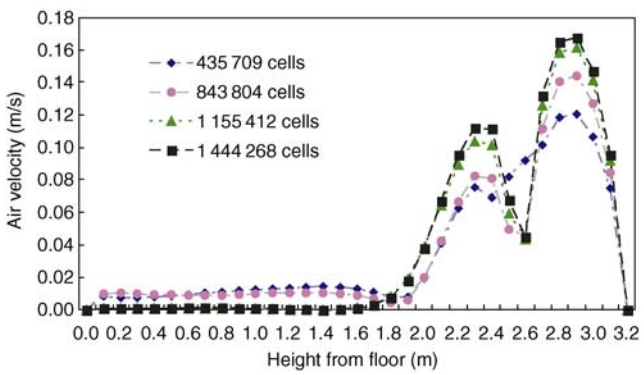

Fig. 4 Grid independent test

directions (that is between tools in the cases of the cleanroom with tools), and 1 000 000 particles each kind of diameter are injected in a linear variation between points (3.9, 1.5, 2.7) and (5.0, 1.5, 2.7) in Cartesian coordinates. All particles are assumed have the same density of 1550 kg/m^3. The "escape" boundary condition is assumed at the outlet boundaries, i.e., defined as having "escaped" when they encounter the boundaries. When particles encounter any wall, they are assumed to be "trapped" on the wall, indicating that the calculation is terminated and the particles remain "attached" to the walls. If the maximum number of time steps, used to compute a single particle trajectory via integration of Eq. (7), is insufficient for completion of the trajectory calculation, the fate for a particle trajectory will be "incomplete". In this case, when trajectories are reported as incomplete within the domain and the particles are not recirculating indefinitely, the maximum number of time steps shall be increased.

4 Results and discussion

4.1 Flow fields

The supply grilles were located over the center of each tool in models A, B, and C, whereas the return grilles were located above a space between the tools, at the low parts of side walls, and at the surroundings of the supply grilles in Figs. 5 – 7, respectively. In order to show airflow fields containing the supply and return grilles, three different locations of plans were cut in Figs. 1 – 3. Since the streamlines of velocity vectors in the red sections, as revealed in Figs. 1 – 3, are symmetric, Fig. 5 shows half the streamlines of velocity vectors at a plan cutting across a diagonal line of the *x*-*z* axle, referring to a red section in Fig. 1, while Figs. 6 and 7 show the ones at the *x*-*y* plans of $z = 6.52$ m and $z = 3.9$ m, referring to the red sections in Figs. 2 and 3, respectively.

In model A (Fig. 5), at the tool coverage ratio of 0%, as shown in Fig. 5(a), the ceiling supply air reached downward to the floor, and then returned upward to the ceiling return grilles. Large recirculation airflows and swirls were generated between the falling and the rising airflows, and resulted in stagnation regions. At the tool coverage ratio of 38%, as shown in Fig. 5(b), when the downward airflow from the supply grilles hit the top surfaces of the tools, the airflow was separated into two horizontal streams (the left and the right). After hitting the top surfaces of the tools on the left, the airflow between the tools and walls were flowing towards the upper return grilles, while the opposite air stream was flowing towards the upper return grilles and flowing downward between the tools. Swirls were created between

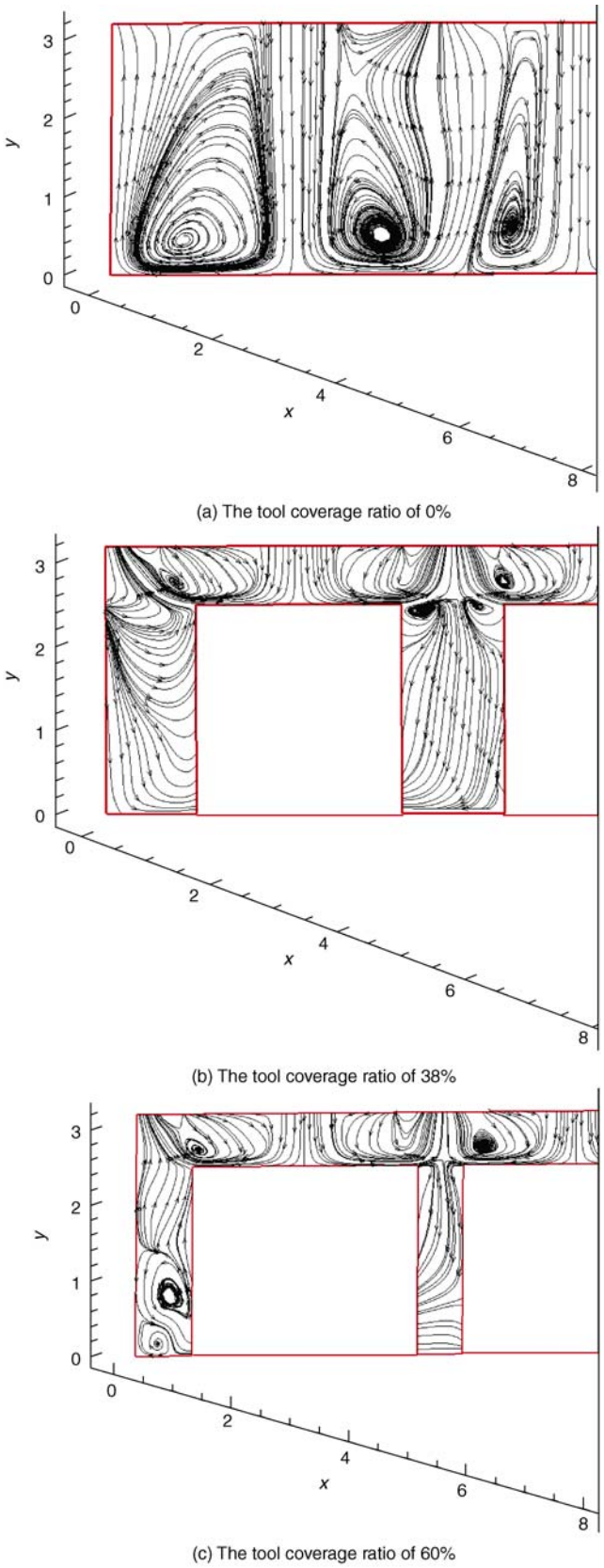

(a) The tool coverage ratio of 0%

(b) The tool coverage ratio of 38%

(c) The tool coverage ratio of 60%

Fig. 5 Streamlines of velocity vectors in model A

tools at a floor height of about 2.5 m, and particles were easily accumulated in the regions because the downward airflows made it difficult to transport particles upward to the ceiling return grilles. At the tool coverage ratio of 60%, as shown in Fig. 5(c), the streamlines of velocity vectors above the floor height of about 2.6 m in Fig. 5(c) were similar to the ones in Fig. 5(b); moreover, swirls were found between the wall and tool at below the floor height of about 1.2 m, and particles were also easily accumulated in the regions. However, it was observed that the rising airflow was also formed between the wall and tool and beneficial in removing particles towards return grilles on the ceiling.

In model B (Fig. 6), at the tool coverage ratio of 0%, as shown in Fig. 6(a), the ceiling supply air downwardly flowed towards the low wall-return grilles near the floor, and a swirl was formed at the left side of this airflow path. Another large swirl was formed between two downward supply jets at below the floor height of about 1 m. Particles in the swirl regions were difficult to be extracted out of the cleanroom. At the tool coverage ratio of 38%, as shown in Fig. 6(b), when the ceiling supply airflow downwardly hit the top surfaces of the tools, the airflow was also divided into two horizontal directions (the left and the right). The left airflow after hitting the top surfaces of the tools was downwardly flowing towards the low wall-return grilles, and resulted in two swirls in a diagonal arrangement at above the floor height of about 1.7 m, while the right airflow after hitting the top surfaces of the tools was downwardly flowing along one side of the tool, and resulted in two large recirculation airflows in a diagonal arrangement at above the floor height of about 1 m. Particles were easily accumulated between the tools and between two supply grilles, due to the occurrence of swirls and large recirculation airflows. At the tool coverage ratio of 60%, as shown in Fig. 6(c), the streamlines of velocity vectors in Fig. 6(c) were similar to the ones in Fig. 6(b). Swirls and recirculation airflows were formed at above the floor height of about 1.6 m.

In model C (Fig. 7), at the tool coverage ratio of 0%, as shown in Fig. 7(a), swirls and large recirculation airflows were formed beside the downward supply air jet. At the tool coverage ratio of 38%, as shown in Fig. 7(b), swirls and large recirculation airflows were formed at above the floor height of about 2 m. Particles hardly escaped from these regions and were easily accumulated in these regions. The airflow between the tools was rising towards the ceiling-return grilles. These rising airflow will carry about particles affected easily by the movement of airflow towards the return grilles. At the tool coverage ratio of 60%, as shown in Fig. 7(c), the streamlines of velocity vectors in Fig. 7(c) were similar to the ones in Fig. 7(b).

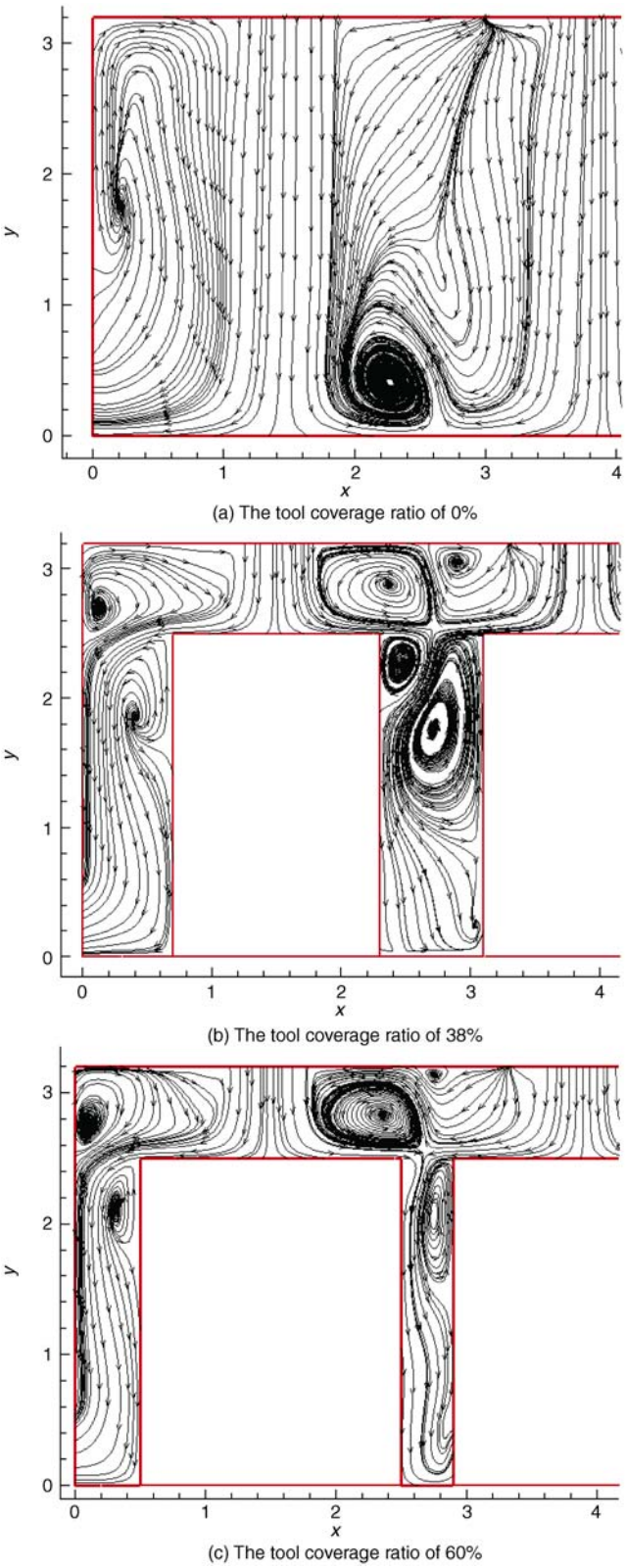

Fig. 6 Streamlines of velocity vectors in model B

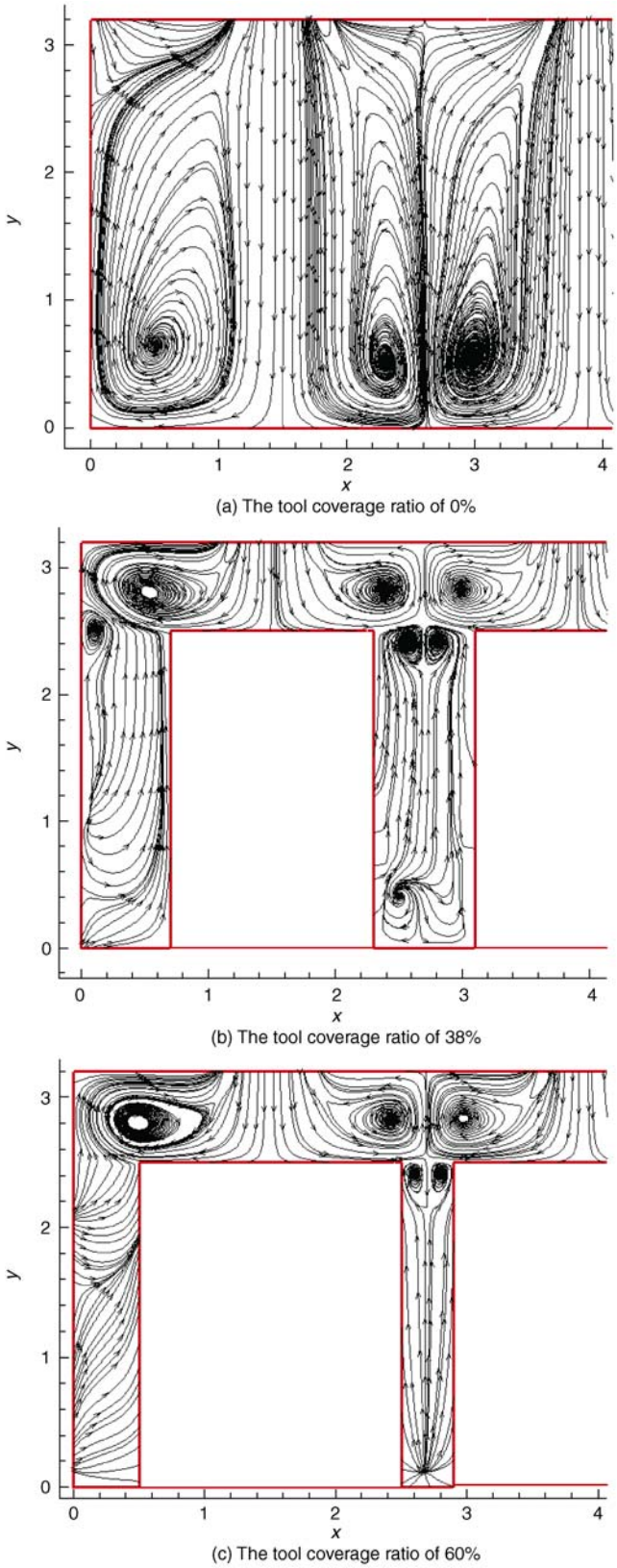

Fig. 7 Streamlines of velocity vectors in model C

4.2 Particle fates

The stochastic tracking model was applied to predict the dispersion of particles, due to the turbulence of airflow. For particles easily affected by the movement of airflow, such as submicron particles, the room airflow had a great impact on particle fates. A particle escaped ratio was defined as the ratio of the numbers of escaped particles to the numbers of released particles. Figures 8 – 10 show the ratios of escaped particles with diameters of 0.01 μm, 0.1 μm, 1.0 μm, 10 μm, and 100 μm, each corresponding to three tool coverage ratios in ventilation models A, B, and C, respectively. A higher number of escaped particles indicated higher particle removal efficiency. Key findings were:

(1) No particles with diameter of 100 μm or larger were removed from the cleanrooms with any of the three tool coverage ratios by any of the ventilation arrangements (A, B, and C). This was because gravitational forces were dominant—making it difficult to remove the large particles from the cleanroom via the ventilation arrangements in this study.

(2) Compared with cleanrooms with higher tool coverage ratios, an empty cleanroom benefited from achieving higher particle removal rates for all three ventilation arrangements (models A, B, and C). For example, the numbers of escaped particles in models B and C were consistently reduced corresponding to the increases in tool coverage ratios (from 0% to 38% then to 60%). This was likely because the large tools blocked the airflow paths in the cleanroom and more particles would be trapped by the eddies that made it difficult for particles to escape. On the contrary, when the tool coverage ratio increased from 38% to 60%, the escaped particles in model A exhibited a reversed trend—the removal rate actually increased instead. In this ventilation mode, the higher tool coverage ratio (i.e., 60%) actually have reduced the eddies that were associated with the lower tool coverage ratio (i.e., 38%), which presented barriers against the particles designed to move towards the upper return grilles of the cleanroom.

(3) For the empty cleanroom (tool coverage ratio of 0%, as shown in Fig. 8), the percentage of the escaped particles $\leqslant$10 μm diameter in models A, B, and C were 70% – 71%, 41% – 45%, and 71% – 77%, respectively. For particles $\leqslant$10 μm in diameter, particle removal efficiency using ventilation arrangement B in the empty cleanroom was lowest among all three arrangements. The number of escaped particles in model A or C was about 1.7 times the one in model B. It may be that the model B had only four return grilles located on the side walls, while the return grilles in models A and C were uniformly distributive; hence, particles far away from the wall return grilles in model B were hardly extracted. Moreover, since models A and C featured the

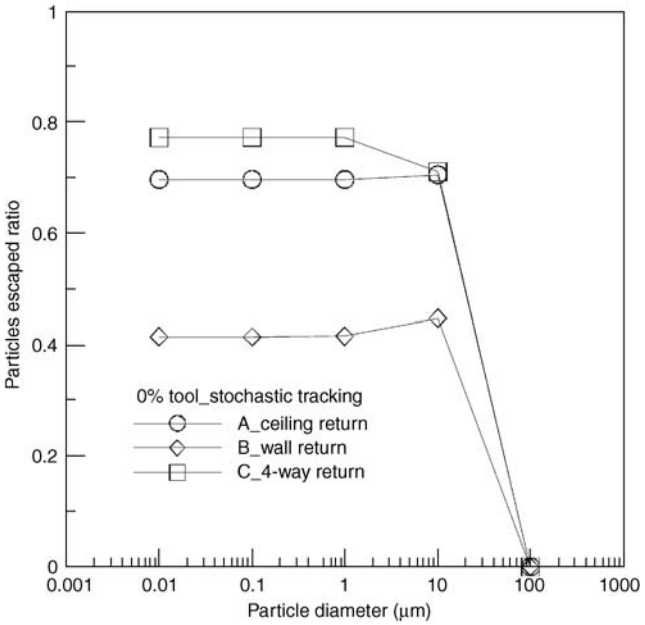

Fig. 8 Ratios of the escaped particles at the tool coverage ratio of 0% in models A, B, and C

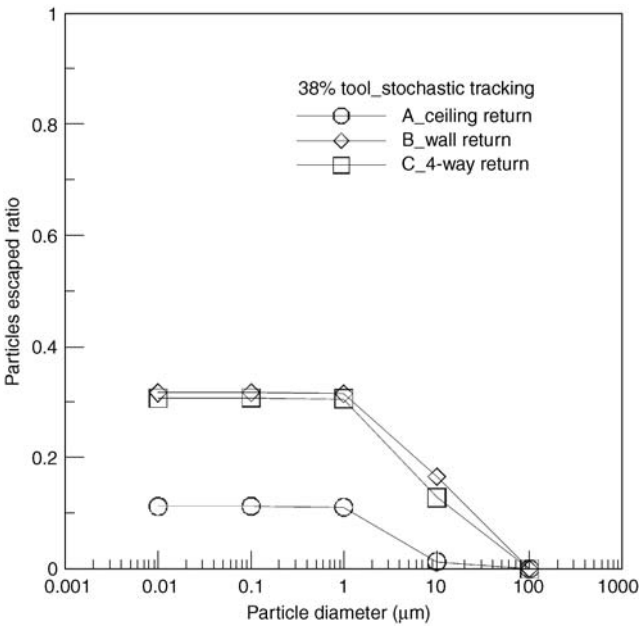

Fig. 9 Ratios of the escaped particles at the tool coverage ratio of 38% in models A, B, and C

locally balanced flow rates of the supply and return air, they had the better effect on the removal of particles than model B in the empty cleanroom; whereas model B could not feature the locally balanced airflow rate, as the return grilles were located on the side walls and not locally around each ceiling supply grille.

(4) For the cleanroom with moderate tool coverage (tool coverage ratio of 38%, as shown in Fig. 9), the percentage of the escaped particles $\leqslant$1.0 μm diameter in models A, B, and C was 11%, 32%, and 31%, respectively, while the one of 10 μm diameter in models A, B, and C was 1%, 17%, and 13%, respectively. In this cleanroom setting, ventilation arrangements B and C exhibited higher particle removal efficiency than ventilation arrangement A. This was because significantly more swirls were generated between the tools and blocked particles from being removed via the ceiling return grilles, and the room airflow was mostly downward and against removing particles towards the upper return grilles. As for models B and C, there was no significant difference in removing submicron particles. Model B or C had larger escaped particles $\leqslant$1.0 μm diameter than model A by about 2.8 times in the cleanroom with slight tool coverage ratio at 38%.

(5) For the cleanroom with high tool coverage (tool coverage ratio of 60%, as shown in Fig. 10), the percentage of the escaped particles $\leqslant$1.0 μm diameter in models A, B, and C was 31% − 32%, 21%, and 7%, respectively, while the one of 10 μm diameter in models A, B, and C was 0.6%, 5.3%, and 1.3%, respectively. Model A exhibited highest particles removing rate for the particles that were no larger than 1.0 μm in diameter but had the lowest removal efficiency

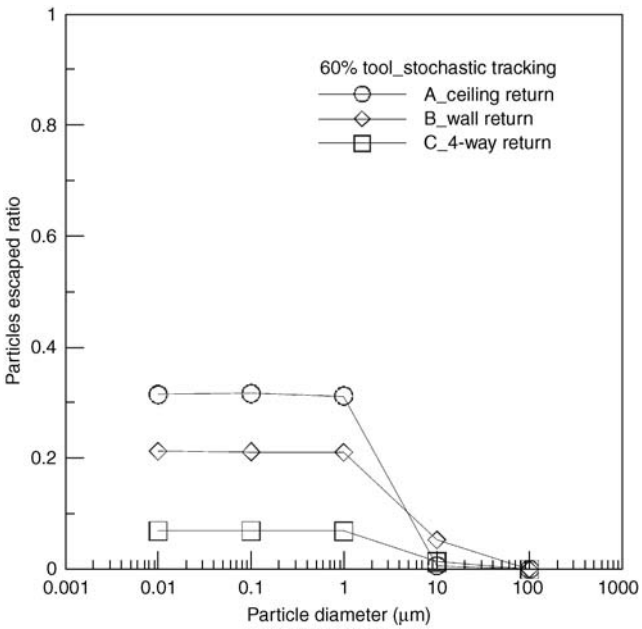

Fig. 10 Ratios of the escaped particles at the tool coverage ratio of 60% in models A, B, and C

for particle of 10 μm in diameter. For the removal of particles $\leqslant$1.0 μm diameter, model A was at a rate of about 1.4 and 4.5 times greater than models B and C in the cleanroom with large tool coverage ratio, respectively. This was likely because the model A created least amount of swirls compared with two other models for submicron airborne particles. Both model A and C become ineffective to remove larger particles via the ceiling due to more dominant gravitational forces. Moreover, the downward airflow between

the tools in model A helped the larger particles settle down on the floor and resulted in the worst removal of particles.

5 Conclusions

The present study employ CFD to qualitatively and quantitatively investigate the streamlines of velocity vectors and the fates of particles of diameters 0.01 μm, 0.1 μm, 1.0 μm, 10 μm, and 100 μm in cleanrooms with three different ventilation arrangements and three levels of tool coverage ratios. The three ventilation arrangements are locally balanced ceiling-return, wall-return, and four-way ceiling-return respectively to maintain contamination control for non-unidirectional airflow cleanrooms with air change rates above the minimal value (20 ACH) recommended for ISO cleanliness class 7. Results indicate that increasing tool coverage ratios in the cleanrooms has an adverse impact on the efficiency in particle removal from the cleanrooms in all ventilation arrangements. Second, the arrangements of locally balanced ceiling-return, wall-return, and four-way ceiling-return ventilation models can effectively remove particles no more than 1.0 μm in diameter for the tool coverage ratios of 60%, 38%, and 0%, respectively. For removing 10 μm diameter particles from the empty cleanroom, three ventilation models exhibited similar efficiency to those of submicron particles; whereas all the ventilation models become essentially ineffective to remove when the tool coverage ratios are above 38%. In addition, particles larger than 100 μm in diameter would not be removed effectively using any of the ventilation schemes studied in this paper. It is recommended that detailed study should be performed when selecting and identifying optimal ventilation design, taking into account of cleanroom size, cleanliness level, sizing of ventilation system, air change rate, along with tool coverage requirements. The results presented in this paper are subject to the airflow characteristics ignoring the energy effects. Future researchers may like to expand the air distribution and particle fate to cover the energy issues and others, such as the supply air temperature, heating source, and tools' surface temperature and height.

References

Chang TJ, Hsieh YF, Kao HM (2006). Numerical investigation of airflow pattern and particulate matter transport in naturally ventilated multi-room buildings. *Indoor Air*, 16: 136 – 152.

Chen JJ, Lan CH, Jeng MS, Xu T (2007). The development of fan filter unit with flow rate feedback control in a cleanroom. *Building and Environment*, 42: 3556 – 3561.

Chen Q (1995). Comparison of different *k-ε* models for indoor air flow computations. *Numerical Heat Transfer, Part B: Fundamentals*, 28: 353 – 369.

Cheng WC, Liu CH, Leung Dennis YC (2009). On the comparison of the ventilation performance of street canyons of different aspect ratios and Richardson number. *Building Simulation*, 2: 53 – 61.

Cheong KWD, Phua SY (2006). Development of ventilation design strategy for effective removal of pollutant in the isolation room of a hospital. *Building and Environment*, 41: 1161 – 1170.

Feziger JH, Peric M (2002). Computational Methods for Fluid Dynamics, 3rd edn. Berlin, New York: Springer.

Fluent Inc (2004). Computational Fluid Dynamics Software, 6.1 edn. Lebanon, New Hampshire, Fluent Inc.

Hu SC, Tung YC (2002). Performance assessment for locally balanced and wall-return turbulent clean rooms by the stochastic particle tracking model. *International Journal on Architectural Science*, 3(4): 146 – 162.

IEST-RP-CC012.2 (2007). Considerations in Cleanroom Design. The Institute of Environmental Sciences and Technology (IEST), IL, USA.

International Organization for Standardization (ISO) (1999). ISO 14644-1, Cleanrooms and Associate Controlled Environments—Part 1 Classification of Air Cleanliness. The Institute of Environmental Sciences and Technology (IEST). IL, USA.

Kassomenos P, Karayannis A, Panagopoulos I, Karakitsios S, Petrakis M (2008). Modelling the dispersion of a toxic substance at a workplace. *Environmental Modelling & Software*, 23: 82 – 89.

Kato S, Murakami S, Nagano S (1992). Numerical study on diffusion in a room with a locally balanced supply-exhaust air flow rate system. *ASHRAE Transactions*, 98(1): 218 – 238.

Kim CN, Choi WH, Choung SJ, Park CH, Kim DS (2002). Efficient ventilation of VOC spread in a small-scale painting process. *Building and Environment*, 37: 1321 – 1328.

Lu W, Howarth AT (1996). Numerical analysis of indoor aerosol particle deposition and distribution in two-zone ventilation system. *Building and Environment*, 31: 41 – 50.

Murakami S, Kato S, Suyama Y (1989). Numerical study on diffusion field as affected by arrangement of supply and exhaust openings in conventional flow type clean room. *ASHRAE Transactions*, 95(2): 113 – 127.

Patankar SV (1980). Numerical Heat Transfer and Fluid Flow. Hemisphere, Washington, D.C.

Shimada M, Okuyama K, Okazaki S, Asai T, Matsukura M, Ishizu Y (1996). Numerical simulation and experiment on the transport of fine particles in a ventilated room. *Aerosol Science and Technology*, 25: 242 – 255.

Wang H, Wang Z, Liu C (2006). Hot air stratification of ceiling air supply in a large space building. ICEBO 2006, Shenzhen, China.

Xu T, Lan CH, Jeng MS (2007). Performance of large fan-filter units for cleanroom applications. *Building and Environment*, 42: 2299 – 2304.

Yang C, Yang X, Xu T, Sun L, Gong W (2009). Optimization of bathroom ventilation design for an ISO Class 5 clean ward. *Building Simulation*, 2: 133 – 142.

Yi YK, Malkawi AM (2008). Site-specific prediction for energy simulation by integrating computational fluid dynamics. *Building Simulation*, 1: 270 – 277.

Zhai Z, Gao Y, Chen Q (2004). Pressure boundary conditions in multi-zone and CFD program coupling. SimBuild 2004, IBPSA-USA National Conference Boulder, CO.

Zhang Z, Chen Q (2006). Experimental measurements and numerical simulations of particle transport and distribution in ventilated rooms. *Atmospheric Environment*, 40: 3396 – 3408.

Zhao B, Wu J (2005). Numerical investigation of particle diffusion in a clean room. *Indoor and Built Environment*, 14: 469 – 479.